Occultation of a Large Star by the Large Plutino (28978) Ixion on 2020 October 13 UTC

Stephen E. Levine[1,2] , Carlos A. Zuluaga[2], Michael J. Person[2] , Amanda A. Sickafoose[2,3] , Amanda S. Bosh[1,2] , and Michael Collins[1]

[1] Lowell Observatory, 1400 West Mars Hill Road, Flagstaff, AZ 86001, USA; sel@lowell.edu
[2] Department of Earth, Atmospheric and Planetary Sciences, Massachusetts Institute of Technology, 77 Massachusetts Avenue, Cambridge, MA 02139, USA
[3] Planetary Science Institute, 1700 East Fort Lowell, Tucson, AZ 85719, USA
Received 2021 January 5; revised 2021 February 16; accepted 2021 February 16; published 2021 April 7

Abstract

We observed the occultation of the star Gaia DR2 4056440205544338944 by (28978) Ixion. The event was observed from two Lowell Observatory sites, using the 4.3 m Lowell Discovery Telescope (LDT), near Happy Jack, AZ, USA, and a 0.32 m telescope co-mounted with the Titan Monitoring telescope on Lowell's Mars Hill campus in Flagstaff, AZ. The LDT chord, at 44.86 s, was roughly 30% longer than the longest predicted possible chord. Under the assumption of a spherical body, Ixion's fitted diameter $D = 709.6 \pm 0.2$ km. The LDT light-curve profile was used to place an upper limit on the surface pressure $P < 2\ \mu$bar on any possible atmosphere of Ixion. At the distance of Ixion, the occulted star had a fitted projected diameter of 19.25 ± 0.3 km assuming uniform disk illumination, giving a stellar angular diameter of 0.675 ± 0.010 mas. Using the Gaia EDR3 parallax of 0.565 mas, the stellar radius is $130^{+20}_{-17}\ R_\odot$. The measured size is consistent with prior spectral classification of this star as a reddened mid-M giant. This is one of only a modest number of M5 III stars to have a directly measured diameter, and is more distant than most.

Unified Astronomy Thesaurus concepts: Asteroid occultation (71); Stellar occultation (2135); Trans-Neptunian objects (1705); High angular resolution (2167)

1. Introduction

Stellar occultations have proven to be one of the most accurate techniques for measuring physical characteristics of trans-Neptunian objects (TNOs). The first successful occultation observation by a TNO other than Pluto or Charon was in 2009 (55636; Elliot et al. 2010). Since then, stellar occultations by multiple TNOs have returned sizes at kilometer scale (e.g., Dias-Oliveira et al. 2017; Buie et al. 2020a, 2020b; Leiva et al. 2020; Souami et al. 2020), placed nanobar-level constraints on atmospheres (e.g., Sicardy et al. 2011; Braga-Ribas et al. 2013), and detected and characterized rings around three objects (e.g., Braga-Ribas et al. 2014; Bérard et al. 2017; Ortiz et al. 2017; Sickafoose et al. 2020). All of these occultation observations are challenging, given the small angular sizes of the occulting bodies (on the order of 10 mas). Here, we report on observations of a stellar occultation by the TNO (28978) Ixion of a bright star as observed from the western United States in 2020.

Ixion has an orbital semimajor axis of 39.8 au with eccentricity 0.25 and inclination 19°.6 (retrieved from JPL Horizons). It is classified as a Plutino, orbiting in the 3:2 resonance with Neptune. Previous size estimates for Ixion include upper limits of 804 and 822 km (Altenhoff et al. 2004; Grundy et al. 2005), 650^{+260}_{-220} km (Stansberry et al. 2008), and 617^{+19}_{-20} km most recently determined from multiband thermal data (Lellouch et al. 2013). A previous occultation detection returned a single chord of 9 ± 1.5 s, corresponding to a minimum diameter of approximately 220 km (Barry et al. 2015).

Ixion has higher albedo than typical TNOs, at >0.15 (Altenhoff et al. 2004) or 0.14 ± 0.011 (Lellouch et al. 2013). Its rotation period is nominally 12.4 ± 0.3 hr. However, the level of photometric variation was low, and the measurement uncertainties were almost as large as the variation, making the period determination difficult. The low photometric variation could be suggestive of a spherical body and/or low albedo differences, or possibly a pole-on orientation (Galiazzo et al. 2016). Near-infrared spectra are featureless, with the observations suggesting that the surface is highly evolved due to long-term irradiation (Licandro et al. 2002). Combined visible-wavelength spectroscopy and polarimetry has shown that Ixion is moderately red with opposition brightening similar to other bodies in the solar system (Boehnhardt et al. 2004). The surface is possibly an areal mixture of the dark and bright compounds amorphous carbon, ice tholin, titan tholin, and water ice (Boehnhardt et al. 2004). Visible-wavelength spectra further show a weak absorption feature at 0.8 μm that could be attributed to aqueous alteration (Marchi et al. 2003).

We observed a stellar occultation by Ixion of a relatively bright star on 2020 October 13. From these data, we derive a new lower limit on Ixion's size and place a constraint on a global atmosphere. We also determine the size of the occulted star. Section 2 contains a description of the occultation prediction, the observations and analyses are presented in Section 3, and there is a discussion in Section 4.

2. Prediction

An occultation of the $G = 10.3$ mag star (Gaia DR2 4056440205544338944) by Ixion was predicted for the night of 2020 October 13 UTC. Parameters relevant to the event are provided in Tables 1 and 2. The occultation star was located in a crowded region within 1°.3 of the Galactic center. From the U.S., the star was quite low in the sky (18° elevation at event

Table 1
Occultation Star Information

Parameter (1)	GDR2 Value[a] (2)	GEDR3 Value[b] (3)	Notes (4)
Epoch [yr]	2015.5	2016.0	
Designation	4056440205544338944	4056440205544338944	
α	$17^{h}50^{m}20\overset{s}{.}36 \pm 0.10$ mas	$17^{h}50^{m}20\overset{s}{.}36 \pm 0.04$ mas	
δ	$-29°43'33\overset{''}{.}1 \pm 0.09$ mas	$-29°43'33\overset{''}{.}1 \pm 0.03$ mas	
μ_{α} [mas yr^{-1}]	0.4 ± 0.2	0.23 ± 0.05	
μ_{δ} [mas yr^{-1}]	0.7 ± 0.1	0.27 ± 0.03	
parallax [mas]	0.769 ± 0.108	0.565 ± 0.042	
l [deg]	359.8	359.8	
b [deg]	-1.3	-1.3	
$T_{\rm eff}$ [K]	3294.0	…	
G [mag]	10.3	10.3	
BP [mag]	12.7	12.7	
RP [mag]	8.9	8.9	
Star photometric data from other sources			
B [mag]	13.6	14.5	APASS[c], NOMAD[d]
V [mag]	12.3		APASS[c]
J [mag]	6.4		2MASS[e]
H [mag]	5.4		2MASS[e]
K [mag]	4.9		2MASS[e]

Notes.
[a] Gaia Data Release 2—Gaia Collaboration et al. (2018), Lindegren et al. (2018).
[b] Gaia Early Data Release 3—Gaia Collaboration et al. (2020).
[c] AAVSO Photometric All Sky Survey, Data Release 10—Henden et al. (2018).
[d] Naval Observatory Merged Astrometric Dataset—Zacharias et al. (2004).
[e] Two Micron All Sky Survey—Skrutskie et al. (2006).

Table 2
Occultation Prediction

Object (1)	Value (2)	Notes (3)
Ixion at the time of the occultation		
Earth—Ixion Distance	39.257 au	From JPL Horizons[a]
Estimated V Magnitude	19.7 mag	From JPL Horizons[a]
Lunar elongation	120deg	
Lunar illumination	below the horizon	
Predicted Ixion—Geocenter close approach distance		
Angular Separation	163.9 ± 49.6 mas	1σ uncertainty
Position Angle	-4.57 deg	Measured North through East
Predicted Midtime	$01^{h}57^{m}55^{s} \pm 65^{s}$ UTC	2020 Oct 13 UTC
Close Approach Distance[b]	-4665 km	
Impact velocity	16.12 km s^{-1}	
Predicted Ixion—LDT close approach distance		
Predicted Midtime	$02^{h}01^{m}18^{s} \pm 65^{s}$ UTC	2020 Oct 13 UTC
Close Approach Distance[b]	$+409$ km	
Impact velocity	15.82 km s^{-1}	
Ixion altitude	18°2	

Notes.
[a] Computed for the time of the occultation by JPL Horizons (https://ssd.jpl.nasa.gov/horizons.cgi).
[b] The close approach sign convention is defined such that positive is the case where the right-handed cross product of the direction of the body motion along the shadow path center line and the direction from the center line to the observing site at close approach is pointed away from the Earth's center. Negative sign has the third axis pointing toward the Earth's center.

midtime, and setting) and the observations were taken starting during nautical twilight. This geometry and crowding in the field were not conducive to obtaining pre- or post-event data in which the star and Ixion were well separated.

TNOs have orbits with long periods, and the archive of observations used to compute their orbits covers only a modest fraction of a single orbit. Largely because of the short arc of observations, the uncertainties in the JPL ephemerides for TNOs are larger than for objects with better orbital coverage. This combination of factors makes it difficult to accurately predict the location of an object like Ixion's shadow path on the Earth.

In an effort to improve our occultation prediction for Ixion, our occultation astrometry group has been performing astrometric observations for the past several years utilizing the 4.3 m Lowell Discovery Telescope (LDT) and the 61 inch Strand Astrometric Reflector at the U.S. Naval Observatory Flagstaff Station (USNOFS), Flagstaff, AZ. Astrometric observations at LDT were taken using the Large Monolithic Imager (LMI), a $6k \times 6k$ e2v CCD that has a $12'\!.3 \times 12'\!.3$ field of view (FoV) and a pixel scale of $0''\!.12$ per pixel (Bida et al. 2014). USNOFS 61 inch data were taken with the EEV24 camera, a $4k \times 2k$ e2v CCD, which has a $12' \times 6'$ FoV and a pixel scale of $0''\!.18$ per pixel (Dahn et al. 2017).

All astrometric images were reduced using network stars with reference positions from the Gaia Data Release 2 (DR2; Gaia Collaboration et al. 2018) catalog. Because the LDT is a corrected Ritchey–Chrétien with a relatively wide field, there is a measurable radial third-order term in the plate solution (Levine et al. 2012; DeGroff et al. 2014). To account for small, relatively constant, small-scale, residual aberrations, we also constructed a field-distortion map of the optics generated with millions of data points taken and developed by our astrometry team and applied to
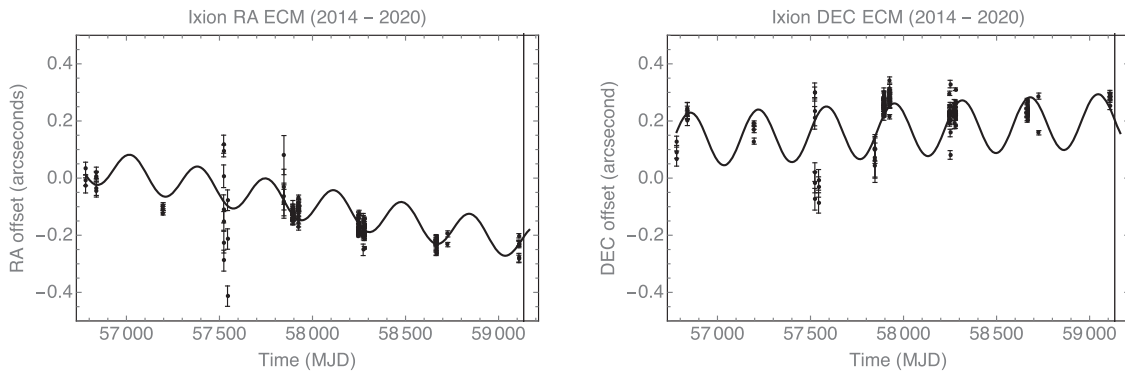
Figure 1. Ephemeris correction model (ECM—solid line) fitted to R.A. (left) and decl. (right) offsets in arcseconds (filled circles) from the predicted Ixion ephemeris over the period 2014–2020. The vertical line at the end of the ECM marks the date and time of the occultation.

the (x, y) plane of the chip. The USNOFS 61 inch reflector has Newtonian optics in a Cassegrain configuration and a relatively slow $f/10$ beam (Strand 1962, 1966). Because of these design aspects, we were able to reduce the data from the 61 inch using linear solutions. We confirmed this by comparing residuals of the reference stars from both linear and higher-order astrometric solutions. These showed no need for higher-order terms in the fit.

Using these measured positions, we have built up ephemeris correction models (ECMs) to aid in predicting occultations by Ixion and a number of other bodies, including the 2011 and 2015 Pluto occultations that were observed with SOFIA (Person et al. 2013, 2021; Zuluaga et al. 2015). These ECMs describe the body's deviation from the JPL ephemeris as a function of time, and they consist of a superposition of Fourier series components. Along with a slope, separate sine and cosine amplitudes are fit instead of a single amplitude and phase because the least-squares fitting is nonlinear with phase. The ECM was propagated forward to the occultation time to calculate Ixion's offsets from the JPL ephemeris (Figure 1).

The predicted path of the event is shown in Figure 2. The shaded parts of the Earth are locations where the Sun is below the horizon. The shadow path for Ixion is shown by solid lines indicating the northern, middle, and southern extent and assuming a diameter of 650 km. The dashed lines indicate the 1σ error in the prediction. In our final prediction, the center line of Ixion's path was 409 ± 1412 km (1σ uncertainty) North of LDT. The Gaia DR2 position was propagated to the time of the occultation and used for the prediction. The DR2 catalog does not include any flags that could potentially affect the prediction (e.g., possible duplicity). Because this occultation star is so close to the Galactic center, precision astrometric measurements run into source confusion problems, which made the final prediction and ECM more uncertain than they would have been in a less crowded field.

3. Observations and Analysis

We observed the occultation from the 4.3 m Lowell Discovery Channel Telescope (LDT) and from a 0.32 m telescope on Lowell Observatory's Mars Hill campus (TiMo).

3.1. LDT

At the LDT (latitude 34:44:39.5N, longitude −111:25:21.1E, altitude 2337 m WGS84, Minor Planet Center observatory code G37) S. Levine and C. Zuluaga observed using RC1, one of the two facility guide and wave front sensing cameras. RC1 is built around an E2V CCD-67 frame transfer CCD with 256×256
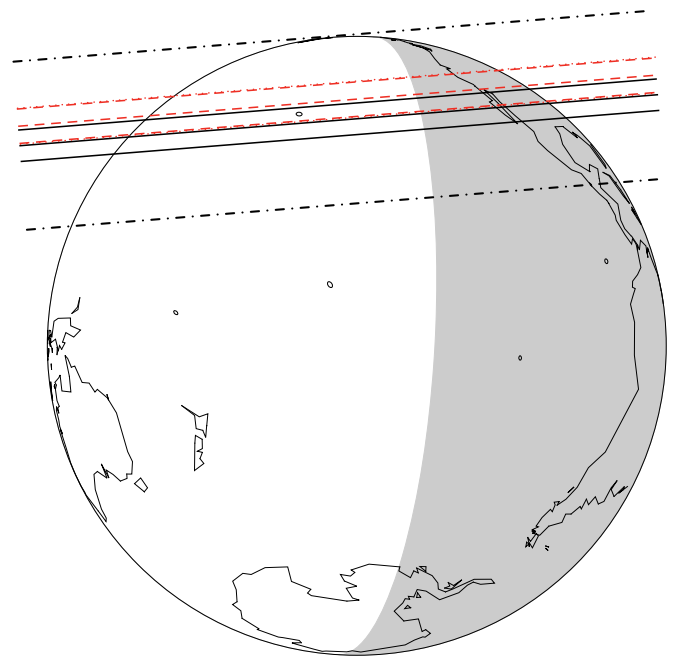

Figure 2. Across the globe pictured, the three solid black lines correspond to the northern limit, center line, and southern limit of Ixion's predicted shadow. The northern and southern limits correspond to a diameter of 650 km. The black dashed–dotted lines indicate 1σ uncertainties. The red dashed lines show the actual path based on the LDT and TiMo detections. The body limits are for a diameter of 710 km. The dotted red lines are the uncertainty due to the uncertainty in the computed close approach distance for LDT. The shaded area on the globe represents where the Sun is below the horizon. The shadow paths on the globe are an approximation at the geocentric close approach time; they disregard the Earth rotation during the event.

pixels each $26 \times 26 \mu m$, and is thermo-electrically cooled to reduce electronic noise. The field of view is $90''$ on a side, and the plate scale is $0''.35$ pixel^{-1}. More details about the system can be found in S. E. Levine et al. (2021, in preparation).

The event was observed unfiltered to maximize signal to noise. The data were taken in occultation mode with a cycle time of 0.3365 s per frame. This included 12.25 ms to shift the data from the integration region to the storage/readout part of the CCD. Timing was handled by the internal timer in the camera controller, which was synchronized to the site GPS/NTP server. The observing run started at 01:47:00.74 UTC and ran for 6232 frames over a period of 35 minutes, roughly centered on the predicted event midtime. The weather during the night was clear. The event occurred roughly 15 minutes
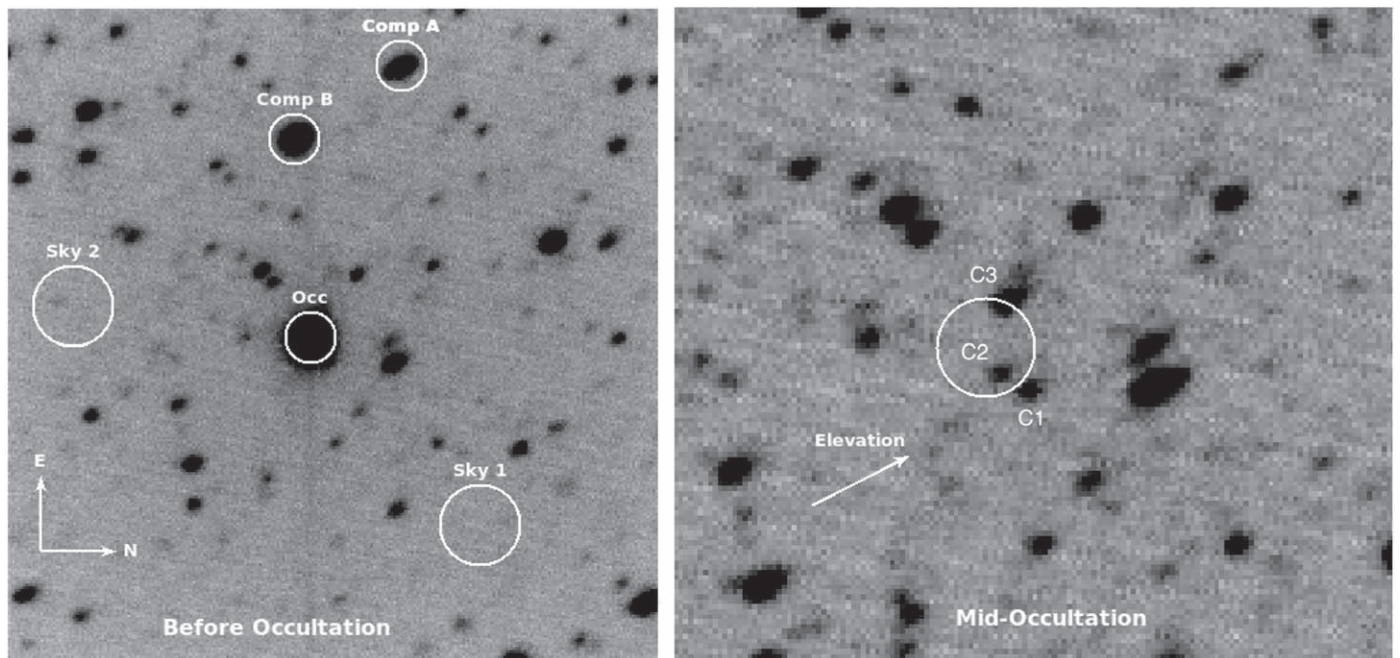
Figure 3. Left: LDT+RC1 occultation field of view ($90'' \times 90''$). The occultation star (Occ), comparison stars A and B, and two sky regions (Sky 1 and Sky 2) are marked. North is to the right, and east is up. Right: zoomed-in view of the location of the occultation star during the occultation. Several faint stars that were otherwise lost in the glare of the brighter star are clearly visible. The white circle marks the photometric aperture. C1, C2, and C3 mark faint stars now visible. C3 is double. The direction of elevation is marked and is roughly parallel to the elongation seen in the stellar images.

before local astronomical twilight at an elevation of roughly 18° as Ixion was setting.

We were able to find two reasonably bright comparison stars within our field of view (Figure 3). We used the first image in the occultation data cube to set the initial positions of the occultation star, two comparison stars (A and B), and two nearby sky regions. We set up nine circular apertures with radii 2, 3, 4, 5, 6, 8, 10, 13, 16 pixels. To centroid the stellar images, we computed the row and column marginal sums for the square box bounding the circular aperture and then computed the image centroid as the first moment of the marginals in x and y. The apertures were then recentered based on this centroid. This was done for each aperture radius for the comp stars on each frame. Centroids from frame N were used as the initial estimate for the centroid locations for frame $N + 1$. For the first 1000 frames, we did the same thing for the occultation star. We then computed the median offset $\Delta(x, y)$ between the two comparison stars' positions and the occultation star. The offsets were then used to predict the occultation star center relative to the comparison stars for all the observation frames. This turned out to be important because of both the loss of occultation star signal during the occultation, and the existence of four faint stars that were hidden in the glare of the occultation star (see the right panel of Figure 3). The LDT tracking was good, and the total range of motion over the 35 minutes observing cube was at most $2\rlap{.}''5$ in each axis making automated extraction straightforward. The sky regions were at fixed positions and their size was that of the largest star aperture (radius = 16 pixels). Within each aperture, we summed the total counts. For the sky apertures, we computed the average sky counts per pixel.

We performed a curve of growth analysis on the first 100 frames in the occultation data set, selecting the aperture closest to, and larger than, the peak signal-to-noise radius. Because of the low elevation, and the brightness of the occultation star, the optimal extraction radius was 10 pixels ($\sim 3\rlap{.}''5$). For the

occultation star and Comp star B, we subtracted off the sky contribution determined from sky 2. For Comp star A, we used the value from sky 1 (see Figure 3). To account for transparency variations, we computed the ratios of the occultation star to Comp B and Comp B to Comp A. The baseline level was determined from the median of the regions outside of the occultation events (see Figure 4). From examination of the images, Comp B looks to be a clean single star; Comp A may be the merge of several stars. For this reason, and because B was the brighter of the two, we used Comp B for the construction of the light curve.

During initial assessments of the data cube we noted that both ingress and egress took place over several images. This type of relatively slow change could be indicative of an atmosphere and/or a relatively large star.

We constructed the event light curve (Figure 4) from the ratio of the occultation star to comp star B, after subtracting median sky values from each. Then we measured the upper and lower baselines and normalized the light curve to range between 1 and 0 during unocculted and fully occulted periods. We extracted an 80 s long subset of the full light curve bracketing the event for analysis. The upper baseline was set by the median value of two regions, each 13.5 s long, one on each side of the event. The upper baseline values agreed to within < 0.1 of the baseline photometry rms scatter. The upper baseline was flat enough that we did not need to correct for a slope in the background. The event zero level was computed from the median of the data during midevent. In addition, we were able to directly estimate what it should have been. The faint stars C1, C2, and C3 marked in Figure 3 (right panel) were visible during the occultation. C1 and C3 are both in the Gaia DR2 catalog. C3 is a double star. We estimate the magnitude of C2 based on C1 (see Table 3). Our estimated upper limit on the flux contribution from Ixion and the C1, C2,
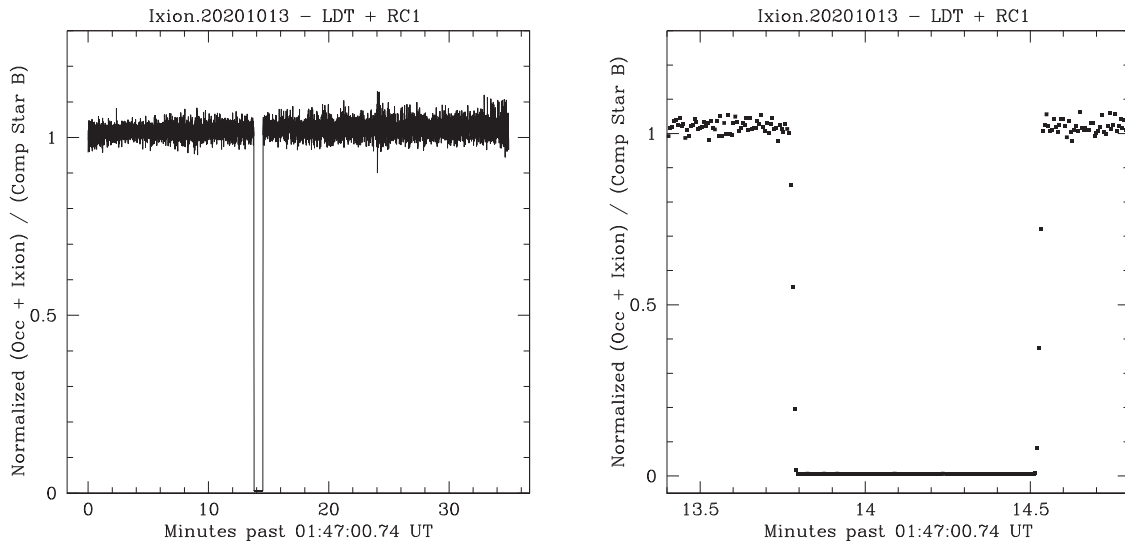
Figure 4. LDT light curve of the occultation by Ixion. Left: the full light curve. Right: expanded view of the Ixion occultation measurements. The light curves are normalized to the ratio of the occultation star plus Ixion divided by a comparison star.

Table 3
Background Star Magnitudes

ID	Gaia DR2 Designation	Gaia G	F_*/F_{occ}
(1)	(2)	(3)	(4)
Occ	4056440205544338944	10.289	1.0
C1	4056440209889613696	16.398	0.0036
C2	···	15.8[a]	0.0063
C3a	4056440209889614848	15.880	0.0058
C3b	4056440209938811904	17.522	0.0013
Ixion	···	19.5[b]	0.0002
Total Residual Flux (upper limit)		···	0.0172

Notes.
[a] Estimated bright magnitude upper limit based on comparison with stars C1 and C3a.
[b] Estimated magnitude based on JPL Horizons predicted V magnitude (19.7), assuming solar colors and using the transformations in Evans et al. (2018).

and C3 stars is 0.0172 of the flux from the occultation star; it should be less because not all of the flux would be in the aperture. This agrees with our fit of the ratio of the zero level to the upper baseline of 0.006.

For the LDT data, we fit a square-well-model (Elliot et al. 1984; Roques et al. 1987) diffraction profile to the primary occultation data. The diffraction profile was convolved to the observed sampling interval of 0.336 s per sample. Given the slow ingress and egress, as expected the fit was not particularly good. Because of the rather extreme red color of the star, we suspected a possibly large projected stellar diameter at the distance of Ixion. Following van Belle (1999), we estimated the likely stellar angular diameter, finding a plausible diameter between 0.2 and 0.7 mas, depending upon assumptions about the stellar details (e.g., type, variability). At the distance of Ixion at the time of the event, the Fresnel scale was roughly 1.4 km (which corresponds to 0.091 s for the impact velocity when observed from LDT), and 1 mas = 28.5 km. We then refit, convolving the diffraction profile with a nonzero diameter star. For a uniform stellar disk, we found a good fit for a

projected stellar diameter at the distance of Ixion of 19.25 ± 0.3 km, or ~0.675 ± 0.010 mas (see Figures 5 and 6, and Table 4). We did not account for possible body curvature on the edge of Ixion. The stellar convolution assumes that the body edge is straight and perpendicular to the impact direction. The star was assumed to be spherical and does not account for the possibility that it might be elliptical due to rotation. We tested simple limb-darkened profiles of the form $I(\theta) = (1 - b) + b \cos(\theta)$, where θ is the angle between line of sight and the normal to the stellar surface (Hanbury Brown et al. 1974; Elliot et al. 1976, 1984). The best-fit limb-darkened model had a projected stellar diameter of 19.5 ± 0.3 km, with a limb-darkening coefficient of $b = 0.15$. Not surprisingly, the limb darkening is positively correlated with the stellar diameter. The ratio of sizes for the limb-darkened to uniform disks is 1.013, which is roughly consistent with that predicted for such a model by Hanbury Brown et al. (1974). The fitted event midtime was within 8 s of the predicted time.

3.2. Lowell Observatory, Mars Hill, Flagstaff, AZ

M. Collins was able to observe the egress from the site of the Titan Monitoring telescope (TiMo) on Lowell Observatory's Mars Hill campus in Flagstaff, AZ (latitude 35:12:07.1N, longitude −111:39:47.9E, altitude 2224 m WGS84, Minor Planet Center observatory code 690). The observations were taken with a 0.32 m diameter, $f/9.0$ telescope, using a Point Grey Blackfly camera (based around the Sony ICX693 CCD), with 808×608 6 μm square pixels. The camera was binned 2×2, giving $0\overset{''}{.}867$ pixels and a full field of view of $5\overset{'}{.}8 \times 4\overset{'}{.}4$. Each exposure time was 0.049 s followed by roughly 750 microseconds readout time. Observations were unfiltered. The image acquisition was done using oaCapture. Due to network connection problems, observations started roughly midway through the occultation at 02:01:14 UTC and were continued through egress. Images were captured in free-run mode and the acquisition software tagged each with the system clock time. During the occultation run, but after the event, a calibration LED was triggered by the GPS unit on the start of each second. From the added illumination in a
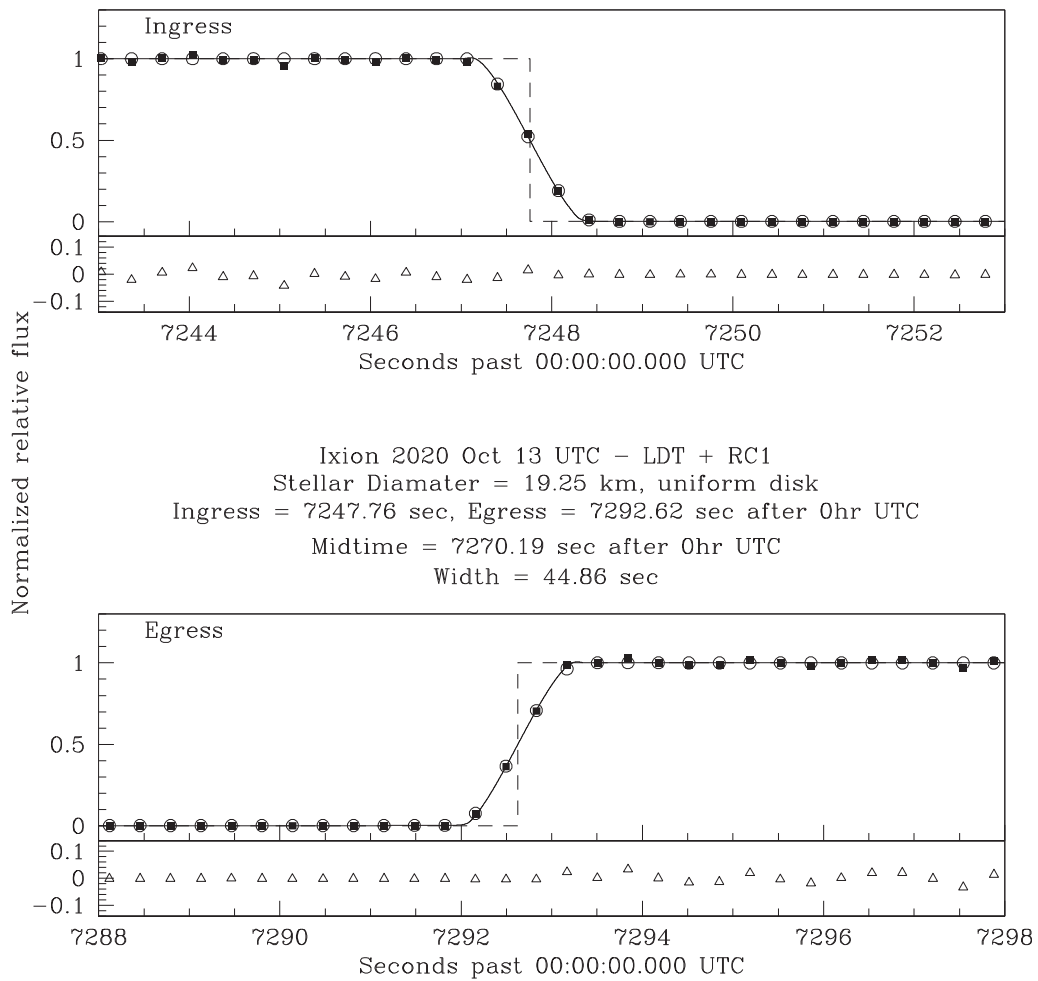
Ixion 2020 Oct 13 UTC − LDT + RC1
Stellar Diameter = 19.25 km, uniform disk
Ingress = 7247.76 sec, Egress = 7292.62 sec after 0hr UTC
Midtime = 7270.19 sec after 0hr UTC
Width = 44.86 sec

Figure 5. Expanded view of ingress and egress, with model fits. Observed data are shown as black squares, open circles are fitted data points, the square-well model is a dashed line, and a diffraction model convolved with a 19.25 km diameter star is the solid line. The open triangle points in the lower panels of each plot are the residuals (data minus convolved diffraction model).
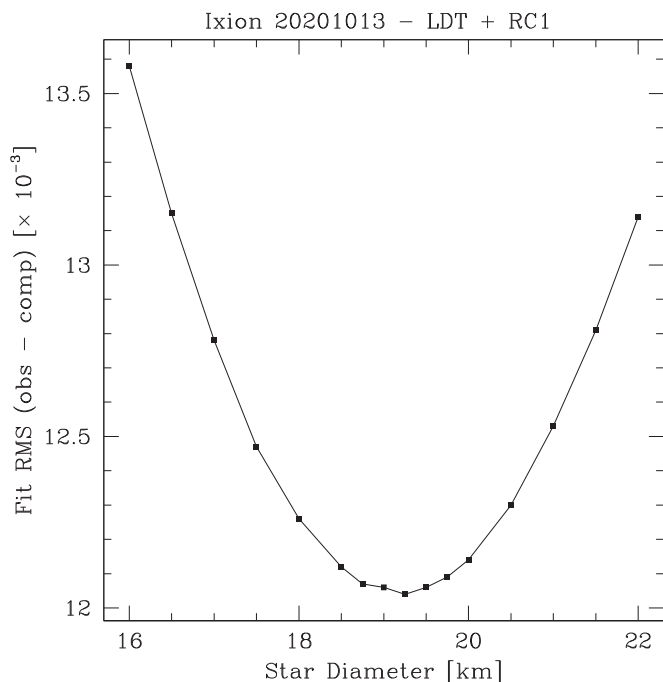
Figure 6. rms (observed minus computed) square-well-model fit residuals as a function of the projected stellar diameter for the LDT light curve.

sequence of 19 such images, the absolute time offset to UTC was determined and applied.

For the Mars Hill data, because the image cadence was high, the signal to noise was relatively low. We were able to detect the occultation star and one comparison star (marked as Comp C in Figure 7) in the raw frames. As a first step in the reduction, we median-combined sets of 10 images to help with the centroiding. In the median-combined images, we were able to easily detect the occultation star and two comparison stars (Comp C and D). We determined centroids for the occultation and comparison stars in the medianed post-event egress frames and computed the offset between the Comp C and occultation star positions. We detected Comp C in all the original frames and placed the occultation star aperture based on the offset previously computed. Initial position estimates for each individual frame were based on the position from the most recent preceding median-combined frame position.

We then followed much the same reduction prescription as for the LDT data. The optimal extraction aperture had a radius of roughly 3″5. Because we only had the egress point, we could not fit a full square well, and instead the egress edge was fit with a knife-edge diffraction profile convolved with a 19.25 km diameter star to get the time of egress (see Figure 8 and Table 4).

Table 4
Occultation Profile Fits

ID	Width (s)	Midtime[a] (s UTC)	Baseline (fraction)	Ingress[a] (s UTC)	Egress[a] (s UTC)	Stellar Diameter[b] (km)
(1)	(2)	(3)	(4)	(5)	(6)	(7)
LDT	44.8640	7270.192	0.002	7247.760	7292.624	19.25
	±0.030	±0.015	±0.003	±0.021	±0.021	±0.3
TiMo	⋯	⋯	0.000	⋯	7290.562	19.25
	⋯	⋯	±0.020	⋯	±0.049	⋯

Notes.
[a] Seconds past 2020-10-13T00:00:00.0 UTC.
[b] Projected stellar diameter at Ixion.
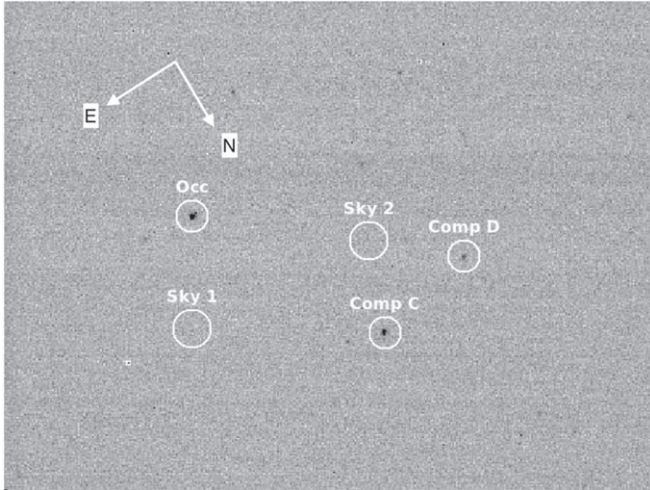
Figure 7. Mars Hill telescope occultation field of view ($5.'8 \times 4.'3$). The occultation star (Occ), comparison stars C and D, and two sky regions (Sky 1 and Sky 2) are marked. The image is the median combination of 10 images from after the end of the event egress.

4. Discussion and Conclusions

We projected the fitted times of ingress and egress from both sites into the (f, g) shadow plane of Ixion, where f and g are parallel to R.A. and decl., respectively, and the plane is perpendicular to the unit vector from the observer to the star (see Section 5.5 of Elliot et al. 1993). This accounts for the displacement between the sites and Ixion's motion. We then fit a circle to the three observed points (see Figure 9). If Ixion were spherical, the nominal body diameter would be $D = 709.6 \pm 0.2$ km. The two chords were close to central with the LDT impact distance ∼5.3 km. The LDT chord length and the two site impact parameters are given in Table 5. Ixion's fitted diameter is consistent with the upper limits of 804 and 822 km of Altenhoff et al. (2004) and Grundy et al. (2005). It is larger than the radii predicted from thermal observations by Stansberry et al. (2008) and Lellouch et al. (2013). The event was also observed by several members of the International Occultation Timing Association in California, Nevada, Arizona, and Texas. They have posted an elliptical body fit based on positive detections from seven sites.[4] Our circular solution,

and all the analysis presented here, is based solely on the data taken from the Lowell sites and is reasonably consistent with their fitted shape of 756.9×684.9 km.

We then fit the LDT data for a possible clear, thin atmosphere (see Figure 10). The surface temperature of $64^{+0.7}_{-1.1}$ K was calculated using a NEATM model (Harris 1998; Lellouch et al. 2013) with beaming factor ($\eta = 0.94^{+0.04}_{-0.06}$) and albedo ($0.14 \pm 0.01$) from the Lellouch "TNOs are Cool" database[5] (Lellouch et al. 2013). Ixion's mass was estimated by assuming a spherical body of diameter 709.6 km, with a mean density similar to that of Charon (1702 ± 21 kg m^{-3}; Stern et al. 2015), and from that we derived the surface gravity. For this temperature and surface gravity, the scale heights for CH_4, H_2O, N_2, CO, and CO_2 range between 72 and 197 km (see Table 6). The thin atmosphere model also requires a differential bending parameter that is equal to the flux residual (for 700 nm light) at the surface (French & Gierasch 1976). Fits were performed at a variety of scale heights spanning those calculated in Table 6, and in all cases, the flux residual value was consistent with 0. The 3σ error bars from these fits were used to place upper limits on possible atmospheric refractivity and thus number density and pressure of the various possible atmospheric components in Table 6. For most plausible constituents based on similar bodies in the outer solar system (CH_4, H_2O, N_2, CO, and CO_2), the 3σ upper limit on detected atmospheric pressure is roughly 0.5 μbar.

Given the relatively small impact distance for the LDT, and assuming that Ixion is spherical, the lack of any brightening in the LDT light curve during the occultation that would be caused by focusing by an atmosphere (like the central flash seen in previous Pluto occultations; e.g., Pasachoff et al. 2017; Person et al. 2021) is also consistent with no atmosphere. If there were an atmosphere, for the fitted impact distance, the lack of central brightening would require an unphysically small atmospheric scale height (significantly less than the impact distance of 5.3 km) and/or very unusually heavy mean molecular weights for constituents of the atmosphere (e.g., for xenon—atomic weight of 131 amu, the scale height would be roughly 24 km; Table 6).

The occultation star is quite red. Based on Gaia DR2, the estimated effective temperature $T_{\rm eff} = 3294$ K (Andrae et al. 2018). Assuming it is a giant, this is consistent with prior spectral classification from Raharto et al. (1984), who classified this as an M5 star. The star has shown possible indications of variability (Haas et al. 2012). Gaia Early Data Release 3
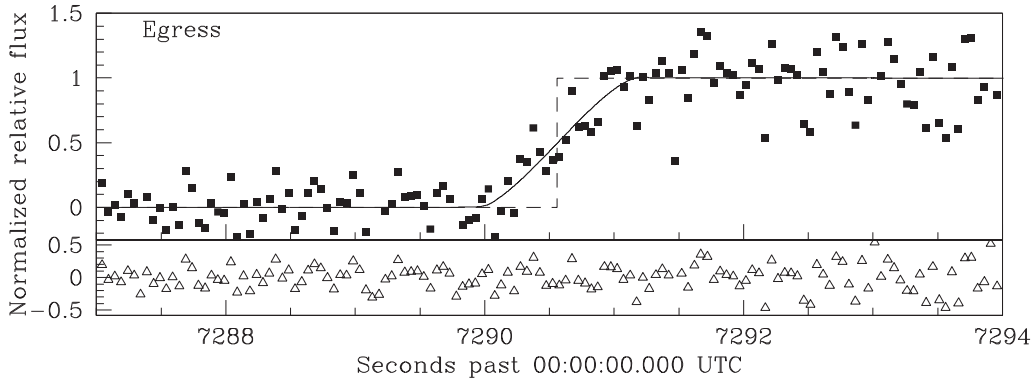
Figure 8. Mars Hill/TiMo site egress, with a diffraction profile model fit. Observed data are shown as black squares, the knife-edge model is a dashed line, and a diffraction model convolved with a 19.25 km diameter star is the solid line. The open triangle points in the lower panel of the plot are the residuals (data minus convolved and sampled diffraction model).
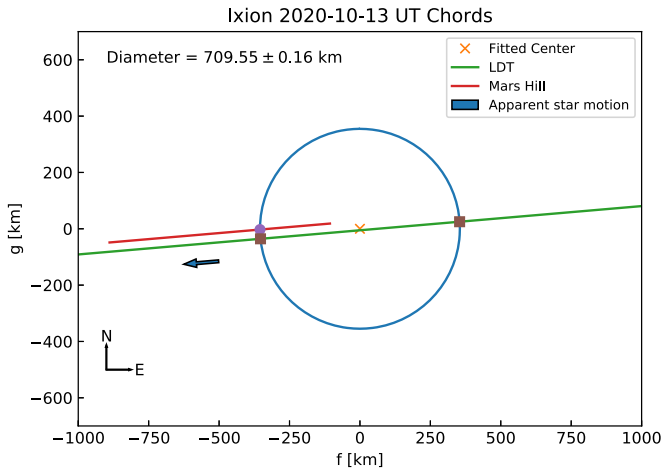

Figure 9. Projection of the occultation chords into the shadow plane of Ixion. The ingress and egress points for each are marked by the heavy dots (square for LDT and circular for Mars Hill). Position uncertainties for the ingress and egress points based on the fitted timings are smaller than the plot markers. The × marks the body center. The best-fit circle diameter to the body is indicated.

Table 5
Occultation Results

ID	Length (km)	Impact Distance (km)[a]
(1)	(2)	(3)
Ixion Diameter	709.6 ± 0.2	…
LDT Chord	709.5 ± 0.4	-5.3 ± 16.7
TiMo Chord	…	27.6 ± 3.2

Note.
[a] Sign convention used to indicate that the two chords are on opposite sides of the body center, with the same sense as used in Table 2, footnote b.

(GEDR3) came out as we were finishing up this manuscript. Here, we give the estimated stellar diameter based on both catalogs. The measured GDR2 parallax is 0.769 ± 0.108 mas. The measured GEDR3 parallax is 0.565 ± 0.042 mas. The parallax is well enough known in both versions that the result of simple inversion to find the distance is consistent with the more sophisticated modeling methods implemented by the Gaia project and made available to the community[6] (Bailer-Jones 2015; Lindegren et al. 2018; Luri et al. 2018). The distance estimated using the Gaia methodology puts the star at a median distance of 1357^{+447}_{-268} pc (GDR2) and 1790^{+243}_{-198} pc (GEDR3), assuming a uniform distance prior; the range is the 90% confidence interval, rather than a 1σ range. We adopted the

uniform distance prior since the star is both relatively close and in the Galactic plane. The median distance estimates for a decreasing space density prior and the frequentist Transform Method of Smith (2000) are 1387 and 1287 pc (GDR2) and 1797 and 1752 pc (GEDR3), respectively.

For each version of Gaia, the estimated distances agree to within ± 70 pc, and bracket the modal estimates as well. The value for the parallax for this star in GEDR3 differs from the value in GDR2 by more than twice the GDR2 parallax formal uncertainty. The proper motion measurements also differ significantly. The GEDR3 measures are presumed to be more accurate because of the increased available data and longer baseline for the astrometric solution (Gaia Collaboration et al. 2020). The star lies very near the line of sight to the Galactic center. Crowding in the field, the projected size of the star (almost a milliarcsecond in diameter), and the late spectral type with possible variability and spots all could combine to account for the variation between the GDR2 and GEDR3 results. The star is also in the bright ($G \leqslant 13$ mag) regime for Gaia and near the Galactic plane where there were known issues in GDR2 with the parallax zero-point solution, and where the formal uncertainties were underestimated (Lindegren et al. 2018).

Combined with the uniform disk fitted projected stellar diameter of 19.25 ± 0.3 km $= 0.675 \pm 0.010$ mas from the LDT occultation light curve, the computed stellar radius is $98^{+35}_{-20} R_{\odot}$ ($78 < R_* < 133 R_{\odot}$) (GDR2) and $130^{+20}_{-17} R_{\odot}$
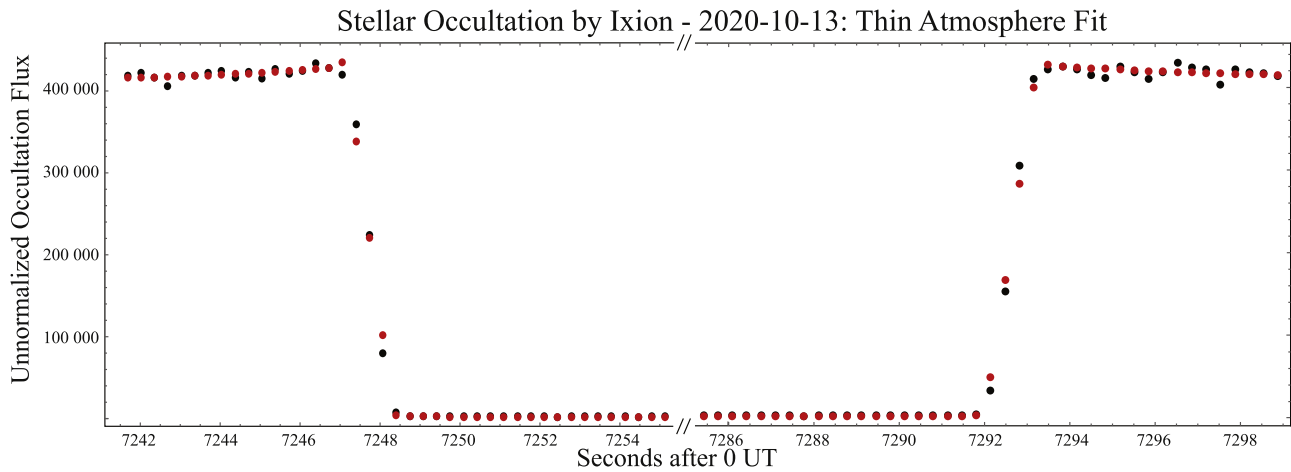
---

[6] Discussion of the methodology and a software implementation are provided by the Gaia team at https://github.com/agabrown/astrometry-inference-tutorials/.

Figure 10. Thin atmosphere model fit to the LDT curve. Here we plot a fit to the LDT occultation light curve (black points). The model (red points) includes a thin isothermal atmosphere (French & Gierasch 1976) of 75 km scale height as well as diffraction effects (Hecht & Zajac 1974) and the finite apparent size of the star (19.25 km), although the model does not include limb darkening. Note that while consistent with photon noise, the residuals between the data and the model during the ingress and egress are all in the proper directions to result from limb-darkening (high above the midpoint and low below the midpoint). The model fit results in an atmospheric flux differential consistent with 0.0 (with some error bar) at all scale heights.

Table 6
Atmospheric Candidate Gases

Molecule	Weight (amu)	Scale Height (km)	Number Density[a] $(10^{13} \text{ cm}^{-3})$	Column Height[a] (cm-amagat)	Surface Pressure[a] (μbar)
(1)	(2)	(3)	(4)	(5)	(6)
CH_4	16.0428	$196.6^{+3.0}_{-3.7}$	5.04	36.9	0.25
H_2O	18.0153	$175.1^{+2.7}_{-3.4}$	8.30	54.1	0.46
Ne	20.1797	$156.3^{+2.4}_{-3.1}$	29.29	170.3	1.80
N_2	28.0134	$112.6^{+1.7}_{-2.2}$	5.66	23.7	0.48
CO	28.0104	$112.6^{+1.7}_{-2.2}$	5.00	20.9	0.43
Ar	39.948	$78.9^{+1.2}_{-1.5}$	4.93	14.5	0.60
CO_2	44.0098	$71.7^{+1.1}_{-1.4}$	2.97	7.9	0.40
Kr	83.8	$37.6^{+0.6}_{-0.7}$	2.27	3.2	0.58
Xe	131.29	$24.0^{+0.4}_{-0.5}$	1.10	1.0	0.44

Note.
[a] 3σ upper limits.

$(114 < R_* < 150 \, R_\odot)$ (GEDR3). The uncertainty in the parallax dominates the uncertainty. This is consistent with the classification as a reddened mid-M giant. It joins a relatively small number of late-type giants with measured stellar diameters (White & Feierman 1987; Nordgren et al. 1999; Baines et al. 2016, 2018) and is later type and more distant (1.7 kpc) than most of the others. The limb-darkened stellar diameter is 0.684 ± 0.010 mas, and the computed physical sizes would scale up by the ratio 1.013 accordingly. For studies of stellar parameters, occultations by asteroids and TNOs can complement measurements by both Lunar occultations and optical and near-IR interferometry.

From this event we have learned that Ixion is 709.6 ± 0.2 km (for a spherical shape), and if it has an atmosphere it is tenuous enough for the surface pressure to be below 3σ upper limits of 0.3–$2 \, \mu$bar, depending upon composition. We have also measured the angular diameter of the occulted star to be 0.675 ± 0.010 mas, which translates to a stellar radius of $130^{+20}_{-17} \, R_\odot$ (GEDR3) at the distance based on the GEDR3 parallax. This is consistent with prior spectral classification showing the star to be a reddened mid-M class giant.

Facilities: LDT(RC1, LMI), USNO:61in(EEV24).

Software: Mathematica (Wolfram Research 2020), matplotlib (Hunter 2007), numpy (Oliphant 2006; van der Walt et al. 2011), scipy (Virtanen et al. 2020).

ORCID iDs

Stephen E. Levine ⬤ https://orcid.org/0000-0002-1050-3539
Michael J. Person ⬤ https://orcid.org/0000-0003-0000-0572
Amanda A. Sickafoose ⬤ https://orcid.org/0000-0002-9468-7477
Amanda S. Bosh ⬤ https://orcid.org/0000-0003-4772-528X

References

Altenhoff, W. J., Bertoldi, F., & Menten, K. M. 2004, A&A, 415, 771
Andrae, R., Fouesneau, M., Creevey, O., et al. 2018, A&A, 616, A8
Bailer-Jones, C. A. L. 2015, PASP, 127, 994
Baines, E. K., Armstrong, J. T., Schmitt, H. R., et al. 2018, AJ, 155, 30
Baines, E. K., Döllinger, M. P., Guenther, E. W., et al. 2016, AJ, 152, 66
Barry, M. A. T., Gault, D., Pavlov, H., et al. 2015, PASA, 32, e031
Bérard, D., Sicardy, B., Camargo, J. I. B., et al. 2017, AJ, 154, 144
Bida, T. A., Dunham, E. W., Massey, P., et al. 2014, Proc. SPIE, 9147, 91472N
Boehnhardt, H., Bagnulo, S., Muinonen, K., et al. 2004, A&A, 415, L21
Braga-Ribas, F., Sicardy, B., Ortiz, J. L., et al. 2013, ApJ, 773, 26
Braga-Ribas, F., Sicardy, B., Ortiz, J. L., et al. 2014, Natur, 508, 72
Buie, M. W., Leiva, R., Keller, J. M., et al. 2020b, AJ, 159, 230
Buie, M. W., Porter, S. B., Tamblyn, P., et al. 2020a, AJ, 159, 130
Dahn, C. C., Harris, H. C., Subasavage, J. P., et al. 2017, AJ, 154, 147
DeGroff, W. T., Levine, S. E., Bida, T. A., et al. 2014, Proc. SPIE, 9145, 91452C
Dias-Oliveira, A., Sicardy, B., Ortiz, J. L., et al. 2017, AJ, 154, 22
Elliot, J. L., Bosh, A. S., Cooke, M. L., et al. 1993, AJ, 106, 2544
Elliot, J. L., French, R. G., Meech, K. J., & Elias, J. H. 1984, AJ, 89, 1587
Elliot, J. L., Person, M. J., Zuluaga, C. A., et al. 2010, Natur, 465, 897

Elliot, J. L., Rages, K., & Veverka, J. 1976, ApJ, 207, 994
Evans, D. W., Riello, M., De Angeli, F., et al. 2018, A&A, 616, A4
French, R. G., & Gierasch, P. J. 1976, AJ, 81, 445
Gaia Collaboration, Brown, A. G. A., Vallenari, A., et al. 2018, A&A, 616, A1
Gaia Collaboration, Brown, A. G. A., Vallenari, A., et al. 2020, arXiv:2012.01533
Galiazzo, M., de la Fuente Marcos, C., de la Fuente Marcos, R., et al. 2016, Ap&SS, 361, 212
Grundy, W. M., Noll, K., & Stephens, D. 2005, Icar, 176, 184
Haas, M., Hackstein, M., Ramolla, M., et al. 2012, AN, 333, 706
Hanbury Brown, R., Davis, J., Lake, R. J. W., et al. 1974, MNRAS, 167, 475
Harris, A. W. 1998, Icar, 131, 291
Hecht, E., & Zajac, A. 1974, Optics (Reading, MA: Addison-Wesley)
Henden, A. A., Levine, S., Terrell, D., et al. 2018, AAS Meeting, 232, 223.06
Hunter, J. D. 2007, CSE, 9, 90
Leiva, R., Buie, M. W., Keller, J. M., et al. 2020, PSJ, 1, 48
Lellouch, E., Santos-Sanz, P., Lacerda, P., et al. 2013, A&A, 557, A60
Levine, S. E., Bida, T. A., Chylek, T. C., et al. 2012, Proc. SPIE, 8444, 844419
Licandro, J., Ghinassi, F., & Testi, L. 2002, A&A, 388, L9
Lindegren, L., Hernández, J., Bombrun, A., et al. 2018, A&A, 616, A2
Luri, X., Brown, A. G. A., Sarro, L. M., et al. 2018, A&A, 616, A9
Marchi, S., Lazzarin, M., Magrin, S., et al. 2003, A&A, 408, L17
Nordgren, T. E., Germain, M. E., Benson, J. A., et al. 1999, AJ, 118, 3032
Ochsenbein, F., Bauer, P., & Marcout, J. 2000, A&AS, 143, 23
Oliphant, T. E. 2006, A Guide to NumPy (Spanish Fork, UT: Tregol Publishing)
Ortiz, J. L., Santos-Sanz, P., Sicardy, B., et al. 2017, Natur, 550, 219
Pasachoff, J. M., Babcock, B. A., Durst, R. F., et al. 2017, Icar, 296, 305
Person, M. J., Bosh, A. S., Zuluaga, C. Z., et al. 2021, Icar, 356, 113572
Person, M. J., Dunham, E. W., Bosh, A. S., et al. 2013, AJ, 146, 83
Raharto, M., Hamajima, K., Ichikawa, T., et al. 1984, AnTok, 19, 469
Roques, F., Moncuquet, M., & Sicardy, B. 1987, AJ, 93, 1549
Sicardy, B., Ortiz, J. L., Assafin, M., et al. 2011, Natur, 478, 493
Sickafoose, A. A., Bosh, A. S., Emery, J. P., et al. 2020, MNRAS, 491, 3643
Skrutskie, M. F., Cutri, R. M., R. Stiening, R., et al. 2006, AJ, 131, 1163
Smith, H., Jr. 2000, in New Developments in the Dynamics of Planetary Systems, ed. R. Dvorak & J. Henrard (Dordrecht: Kluwer), 349
Souami, D., Braga-Ribas, F., Sicardy, B., et al. 2020, A&A, 643, A125
Stansberry, J., Grundy, W., Brown, M., et al. 2008, in The Solar System Beyond Neptune, ed. M. A. Barucci et al. (Tucson: U. of Arizona Press), 161
Stern, S. A., Bagenal, F., Ennico, K., et al. 2015, Sci, 350, aad1815
Strand, K. A. 1962, AJ, 67, 706
Strand, K. A. 1966, VA, 8, 9
van Belle, G. T. 1999, PASP, 111, 1515
van der Walt, S., Colbert, C., & Varoquaux, G. 2011, CSE, 13, 22
Virtanen, P., Gomers, R., Oliphant, T. E., et al. 2020, NatMe, 17, 261
White, N. M., & Feierman, B. H. 1987, AJ, 94, 751
Wolfram Research 2020, Mathematica, v12.2, https://www.wolfram.com/mathematica
Zacharias, N., Monet, D. G., Levine, S. E., et al. 2004, AAS Meeting, 205, 48.15
Zuluaga, C. A., Bosh, A. S., Person, M. J., et al. 2015, AAS/DPS Meeting, 47, 210.13